Front. Phys. 13(4), 134207 (2018)
https://doi.org/10.1007/s11467-018-0803-1

RESEARCH ARTICLE

All-dielectric bowtie waveguide with deep subwavelength mode confinement

Wen-Cheng Yue, Pei-Jun Yao†, Li-Xin Xu, Hai Ming

Department of Optics and Optical Engineering, University of Science and Technology of China, Hefei 230026, China
Corresponding author. E-mail: †yap@ustc.edu.cn
Received March 1, 2018; accepted May 14, 2018

Plasmonic waveguides and conventional dielectric waveguides have favorable characteristics in photonic integrated circuits. Typically, plasmonic waveguides can provide subwavelength mode confinement, as shown by their small mode area, whereas conventional dielectric waveguides guide light with low loss, as shown by their long propagation length. However, the simultaneous achievement of subwavelength mode confinement and low-loss propagation remains limited. In this paper, we propose a novel design of an all-dielectric bowtie waveguide, which simultaneously exhibits both subwavelength mode confinement and theoretically lossless propagation. Contrary to traditional dielectric waveguides, where the guidance of light is based on total internal reflection, the principle of the all-dielectric bowtie waveguide is based on the combined use of the conservation of the normal component of the electric displacement and the tangential component of the electric field, such that it can achieve a mode area comparable to its plasmonic counterparts. The mode distribution in the all-dielectric bowtie waveguide can be precisely controlled by manipulating the geometric design. Our work shows that it is possible to achieve extreme light confinement by using dielectric instead of lossy metals.

Keywords dielectric waveguide, nanophotonics, plasmonics, photonic integrated circuits, silicon

PACS numbers 42.82.Et, 78.67.-n, 71.45.Gm

1 Introduction

Manipulating light at subwavelength scale has great importance in nanophotonics [1]. Strongly confined light at subwavelength scale has a variety of applications, such as optical sensing and switching [2, 3], high-density photonic integrated circuits [4], high-speed and high-sensitivity photonic devices [5], electro-optic modulators [6], compact lasers [7], and polarization control devices [8]. Surface plasmon polariton (SPP) [9, 10] waveguides are among the most promising candidates for large-scale photonic integrated circuits owing to their unique capabilities to break the diffraction limit and to provide tight light confinement at the deep subwavelength scale [10–14]. However, structures based on SPP suffer inevitable high propagation loss due to the metallic ohmic loss [15, 16], despite trying to alleviate losses by the design of hybrid plasmonic waveguides [17–29] and the use of metamaterials [30, 31] and metasurfaces [32]. Conventional dielectric waveguides, such as photonic crystals [33–35], can guide light with low loss; however, they are subject to the diffraction limit in each direction. Although the subwavelength mode confinement has been implemented in all-dielectric coupled silicon waveguides [36–39], it is limited to one dimension, because only the boundary condition on the normal component of the electric displacement is applied.

In this article, by alternately applying the electromagnetic boundary conditions on the normal component of the electric displacement and the tangential component of the electric field, we propose a design process for a novel all-dielectric bowtie (ADB) waveguide and demonstrate the possibility of simultaneously achieving deep subwavelength mode confinement in two dimensions and theoretically lossless propagation in a single all-dielectric waveguide. By manipulating the geometric design of an all-dielectric waveguide, the mode distribution can be flexibly confined in the high-index or low-index regions. Guiding mechanisms based on total internal reflection can only confine light in a high-index material surrounded by a low-index material. Neverthe-

*arXiv: 1706.06724.

less, the guidance of light in a low-index medium also has plenty of applications, such as biosensors [40], avoiding nonlinearity in high-index materials [41], and interaction with low-index materials [33]. A similar design process or a similar dielectric bowtie structure is also applicable to other optical devices, such as the all-dielectric nanocavities designed by the research groups of Weiss and Englund, with a mode volume comparable to its plasmonic counterpart and a quality factor comparable to a traditional photonic crystal cavity [42, 43]. We believe, that in the near future new implementations and applications derived from the dielectric bowtie structure can be introduced.

2 Theoretical background

The mode area (A_{eff}) of an optical waveguide is given by the ratio of the total electromagnetic energy and the maximum electromagnetic energy density as [17],

$$A_{eff} = \frac{1}{\max\{W(\boldsymbol{r})\}} \iint W(\boldsymbol{r}) \mathrm{d}^2\boldsymbol{r}, \tag{1}$$

where $W(\boldsymbol{r})$ is the electromagnetic energy density, while for non-dispersive non-magnetic material

$$W(\boldsymbol{r}) = \frac{1}{2}[\epsilon(\boldsymbol{r})|\boldsymbol{E}(\boldsymbol{r})|^2 + \mu_0|\boldsymbol{H}(\boldsymbol{r})|^2]. \tag{2}$$

Considering the position-dependence of $W(\boldsymbol{r})$, if the maximum electromagnetic energy density is significantly increased at a certain localized position, then the perturbation in the numerator of Eq. (1) is negligible, and the mode area can be reduced significantly. For a slot waveguide, shown in Fig. 1(a) (top), with normalized electromagnetic energy density and electric vector distributions shown in Fig. 1(a) (bottom), the maximum electromagnetic energy density can be increased by confining light into the narrow nanoscale low-permittivity slot region [Fig. 1(a) (bottom)], which is known as the slot effect [36]. The concentration derives from the first electromagnetic boundary condition (denoted by 1st-BC), that is the continuity of the normal component of the electric displacement

$$\epsilon_l E_{n,l} = D_{n,l} = D_{n,h} = \epsilon_h E_{n,h}, \tag{3}$$

$$E_{n,l} = \frac{\epsilon_h}{\epsilon_l} E_{n,h}, \tag{4}$$

where ϵ_h and ϵ_l are the permittivities of high- and low-permittivity materials, respectively. Subscript n represents the normal component of the field, relative to the dielectric boundary. As the electric field is highly polarized perpendicular to the slot [Fig. 1(a) (bottom)], the maximum electric energy density is approximately enhanced by the factor

$$\frac{W_{e1}}{W_{e0}} = \frac{\epsilon_l|\boldsymbol{E}_l|^2}{\epsilon_h|\boldsymbol{E}_h|^2} \approx \frac{\epsilon_l|E_{n,l}|^2}{\epsilon_h|E_{n,h}|^2} = \frac{\epsilon_h}{\epsilon_l}, \tag{5}$$

where W_{e0} and W_{e1} are the maximum electric energy densities in the high-permittivity material and in the slot region of the slot waveguide, shown in Fig. 1(a) (top), respectively. As the slot is narrow, the electric energy density remains high over the whole slot region. Thus, the average electric energy density in the slot can be used to approximately represent the maximum electric energy density and it is greatly increased compared to the maximum electric energy density in a high-permittivity material. As the magnetic field is conservative at the dielectric boundary for non-magnetic materials and varies slowly across the structure, the maximum magnetic energy density is nearly constant compared to that in the high-permittivity material, and can also be represented by the average magnetic energy density in the slot. Therefore, the maximum electromagnetic energy density in the slot, which is approximately equal to the sum of the average electric and magnetic energy densities in the slot, is much higher than that in the high-permittivity material. As the slot is narrow, the integral term in Eq. (1) remains nearly constant. Thus, the mode area is ultimately reduced.

The mode area can be further reduced by applying the second electromagnetic boundary condition on the tangential component of the electric field (denoted by 2nd-BC). Figure 1(b) (bottom) shows the normalized electromagnetic energy density and electric vector distributions for an antislot waveguide, shown in Fig. 1(b) (top), which is constructed by introducing a narrow nanoscale high-permittivity antislot in the slot waveguide, shown in Fig. 1(a) (top). Clearly, the electromagnetic field is mainly confined in the high-permittivity antislot region, known as the antislot effect [43]. This confinement results from the conservation of the tangential component of the electric field at the interface between two materials,

$$E_{t,l} = E_{t,h}, \tag{6}$$

as shown in Fig. 1(b) (bottom, white arrows), where subscript t represents the tangential component of the field with respect to the interface. Compared with the slot waveguide, the maximum electric energy density is approximately increased by the factor

$$\frac{W_{e2}}{W_{e1}} \approx \frac{\epsilon_h|E_{t,h}|^2}{\epsilon_l|E_{t,l}|^2} = \frac{\epsilon_h}{\epsilon_l}, \tag{7}$$

where W_{e2} is the maximum electric energy density in the antislot region of the antislot waveguide, shown in Fig. 1(b) (top). Similarly to the above analysis, the average electric and magnetic energy densities in the antislot

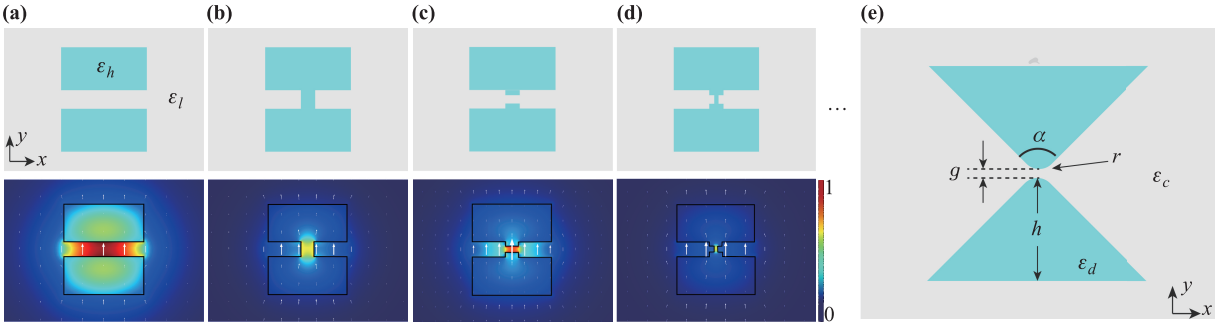

Fig. 1 **(a–d)** Structures (top), normalized electromagnetic energy density and electric vector distributions (bottom) of different waveguide structures, where the slots and antislots are introduced in turn. The width and height of the blue rectangular region are 300 nm and 150 nm, respectively. The width of the slot or antislot is 65 nm, 50 nm, 30 nm, and 15 nm in sequence from (a) to (d). **(e)** Schematic illustration of our proposed ADB waveguide. Two identical dielectric wedges with relative permittivity ε_d are separated by a nanoscale gap of g. The background medium is a dielectric of relative permittivity ε_c. $\varepsilon_d = 12.25$ (Si) and $\varepsilon_c = 2.25$ (SiO_2) at the telecommunications wavelength $\lambda = 1550$ nm. The Si wedge has a height of h, and the wedge tip has an angle of α and its curvature radius is set as $r = 10$ nm [25]. The center of the ADB waveguide defines the origin.

can be used to represent the maximum electric and magnetic energy densities, respectively. The average electric energy density is significantly increased compared to the maximum electric energy density in the slot waveguide, while the average magnetic energy density stays nearly constant. Thus, the maximum electromagnetic energy density is nearly equal to the sum of the average electric and magnetic energy densities in the antislot and it is enhanced compared to the slot waveguide, while the numerator of Eq. (1) remains nearly constant. Thus, the mode area is further reduced.

Combining the 1st-BC and 2nd-BC enables the realization of deep subwavelength mode confinement for an all-dielectric waveguide in two dimensions. As shown in Figs. 1(a)–(d), the alternating introduction of low-permittivity slots (i.e., employing 1st-BC) and high-permittivity antislots (i.e., employing 2nd-BC) can continuously squeeze the mode in y- and x-directions, respectively. The mode is finally confined in the last slot or antislot region. The geometry becomes a bowtie shape in the limit of infinite number of slots and antislots, as shown in Fig. 1(e), while Fig. 1 shows the development of the idea as well.

3 Waveguide structure and mode properties

The designed ADB waveguide is composed of two identical high-permittivity silicon (Si) wedges embedded in a low-permittivity silica (SiO_2) cladding. The separation between the two Si wedges is indicated by g [Fig. 1(e)]. In our study described in the following, we varied the Si wedge height (h), wedge tip angle (α), and the gap distance (g) to control the effective mode area and electromagnetic field distribution of the quasi-TM eigenmode of our ADB waveguide at the telecommunications wavelength ($\lambda = 1550$ nm). The relative permittivities of Si and SiO_2 at $\lambda = 1550$ nm were $\varepsilon_d = 12.25$ and $\varepsilon_c = 2.25$, respectively. The radius of curvature of the wedge tip was $r = 10$ nm [25]. Figure 2(a) shows the dependence of the normalized mode area (A_{eff}/A_0) on h and α at $g = 2$ nm, where A_0 is the diffraction-limited mode area, defined as $\lambda^2/4$, and A_{eff} is calculated by finite element method (FEM) [44]. The normalized mode area decreases at first and then increases with the increasing wedge height for all considered wedge tip angles. For a small wedge height and tip angle ($h < 180$ nm, $\alpha < 80°$), the electromagnetic energy of the quasi-TM eigenmode diffuses in the cladding [Fig. 2(b)], which results in a large mode area [Fig. 2(a)]. Nevertheless, a large wedge height ($h > 300$ nm) results in the spreading of the electromagnetic energy to the Si wedges [Figs. 2(c) and (d)], which also results in a large mode area [Fig. 2(a)]. At medium wedge height (180 nm $< h <$ 300 nm), the electromagnetic energy of the quasi-TM mode is strongly confined within the gap region in two dimensions [Figs. 2(e)–(g)], resulting in a small mode area [Fig. 2(a)]. The white arrows in Figs. 2(e)–(g) indicate the in-plane electric vector distributions of the guided mode of our ADB waveguide. Clearly, the major electric field component is parallel with the y-direction, indicating that the guided mode of the ADB waveguide is a quasi-TM mode. The quasi-TM mode is an eigenmode of the proposed ADB waveguide, and as there are no metal constituents the theoretical loss is zero, which is consistent with the negligible imaginary part of the effective refractive index, calculated by FEM. Interestingly, despite the lossless propagation, the ADB waveguide still provides strong subwavelength mode confinement comparable to its plasmonic counterparts [Fig. 2(a)].

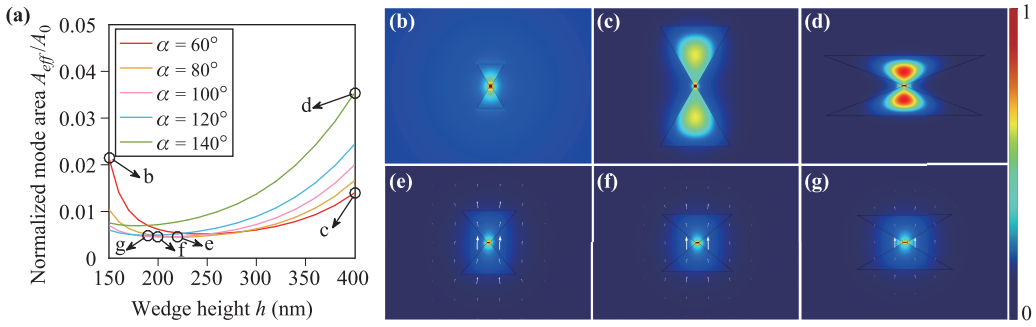

Fig. 2 **(a)** Normalized mode area (A_{eff}/A_0) versus wedge height (h) at different wedge tip angles (α) for g = 2 nm. **(b)–(g)** Normalized electromagnetic energy density distributions for [h, α] = [150 nm, 60°], [400 nm, 60°], [400 nm, 140°], [220 nm, 80°], [200 nm, 100°], and [190 nm, 120°], corresponding to the points indicated in panel (a). The white arrows in (e)-(g) indicate the in-plane electric vector distributions.

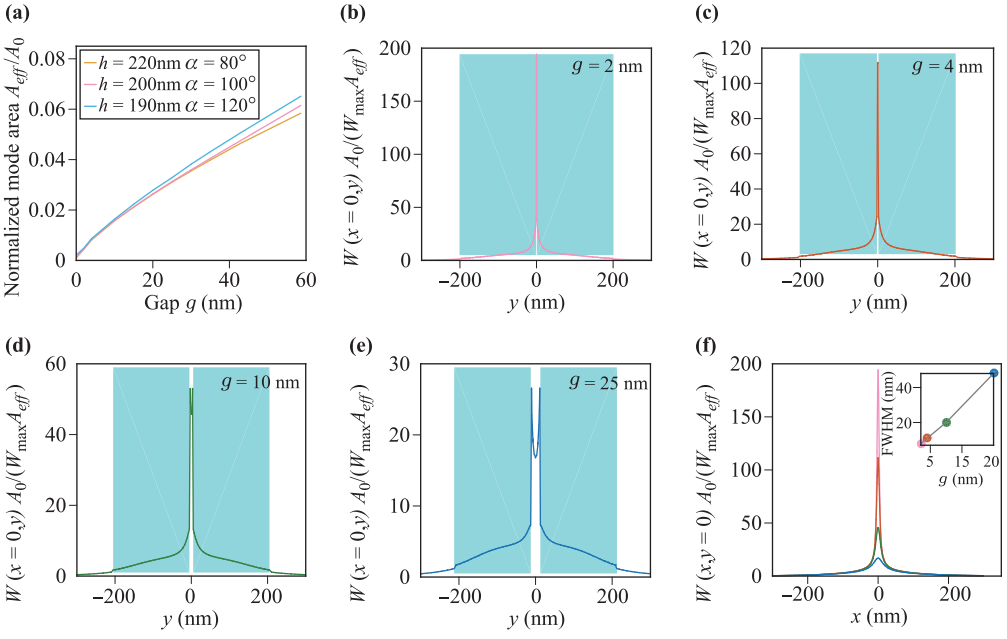

Fig. 3 **(a)** Normalized mode area (A_{eff}/A_0) versus gap (g) for the same set of h and α as in Figs. 2(e)–(g). **(b–e)** Electromagnetic energy density distributions at x = 0 for g = 2 nm, g = 4 nm, g = 10 nm, and g = 25 nm, show the mode confinement in the gap region (no shading). The blue shaded areas represent the region of the two Si wedges. **(f)** Electromagnetic energy density distributions at y = 0 for the same set of g as in (b)–(e) show subwavelength confinement along the x-direction, the inset shows the FWHM of the mode. The parameters in (b)–(f) are h = 200 nm, α = 100°.

Figure 3(a) shows the dependence of the normalized mode area (A_{eff}/A_0) on the gap (g) for the same set of wedge heights (h) and wedge tip angles (α) as in Figs. 2(e)–(g). The normalized mode area increases together with the gap and they achieve their minimum values at g = 0 nm, which corresponds to the case when the ADB waveguide ends with an antislot. The gap stores the electromagnetic energy, enabling subwavelength mode confinement in two dimensions. This can be further verified by the distribution of the electromagnetic energy density at x = 0 or y = 0. The electromagnetic energy density at x = 0 for different gaps is shown in Figs. 3(b)–(e), where the electromagnetic energy density is normalized with respect to the maximum electromagnetic energy density (W_{max}) and the normalized mode area (A_{eff}/A_0). Clearly, the electromagnetic energy density decreases sharply in the region of the two Si wedges, demonstrating a subwavelength mode confinement in the y-direction for all considered g values. Figure 3(f) shows the electromagnetic energy density at y = 0 for the same set of gaps as in Figs. 3(b)–(e). Similarly, the electromagnetic energy density is normalized with respect to

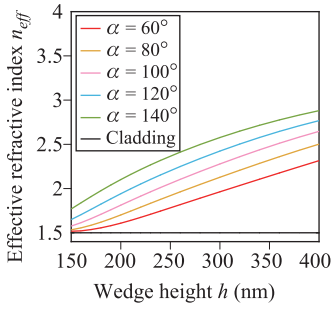

Fig. 4 Effective refractive index (n_{eff}) of the quasi-TM eigenmode versus wedge height (h) for different tip angle (α) when $g = 2$ nm. The black line represents the refractive index of the cladding.

Table 1 Minimum normalized mode areas (A_{eff}/A_0) and the corresponding wedge height (h) for different tip angle (α) at $g = 2$ nm.

α	20°	40°	60°	80°	100°	120°	140°	160°
h (nm)	330	280	240	220	200	190	180	170
A_{eff}/A_0 (10^{-3})	11.2	7.3	5.2	4.5	4.5	4.9	6.9	12.3

the maximum electromagnetic energy density and the normalized mode area. The inset in Fig. 3(f) shows the full-width at half-maximum (FWHM) of the mode. The FWHM is much smaller than the wavelength, indicating a subwavelength mode confinement in the x-direction.

In order to obtain a better understanding, we analyzed the dependence of the effective refractive index (n_{eff}) of the quasi-TM eigenmode on the h and α values at $g = 2$ nm (Fig. 4). The parameters in Fig. 4 are the same as in Fig. 2(a), and the black line in Fig. 4 represents the refractive index of the cladding. The effective refractive index of the quasi-TM eigenmode increases together with the wedge height (h) and tip angle (α). A smaller wedge height and tip angle results in the effective refractive index to become closer to that of the cladding, resulting in diffused electromagnetic energy in the cladding [Fig. 2(b)]. At a certain wedge tip angle, a wedge height, where the mode area is minimal always exists [Fig. 2(a)]. Furthermore, the smaller the tip angle, the larger the corresponding wedge height where the minimum mode area is achieved. Table 1 shows the minimum normalized mode areas and corresponding wedge heights for different wedge tip angle values when $g = 2$ nm. These minimum normalized mode areas are mainly in the order of magnitude of 10^{-3}. When $h = 200$ nm and $\alpha = 100°$ or $h = 220$ nm and $\alpha = 80°$, the smallest normalized mode area of 4.5×10^{-3} can be achieved for $g = 2$ nm, which is approximately 1.3 times smaller than that of the hybrid plasmonic waveguide at the same gap [17]. As the gap distance further decreases ($g \longrightarrow 0$), a much smaller mode area can be expected [Fig. 3(a)].

4 Conclusions

We proposed a novel design for an all-dielectric waveguide. In contrast to the conventional dielectric waveguides, where the guidance of light is based on total internal reflection, the all-dielectric waveguide is designed based on the use of the 1st-BC and 2nd-BC. The alternating use of the 1st-BC and 2nd-BC can continuously squeeze the mode in y- and x-directions, respectively. Eventually, an all-dielectric bowtie waveguide is achieved in the limit of infinite number of interlocked low-permittivity slots (i.e., employing 1st-BC) and high-permittivity antislots (i.e., employing 2nd-BC). The ADB waveguide realized both deep subwavelength mode confinement in two dimensions and a theoretically lossless propagation simultaneously. By manipulating the geometric design, the mode can be flexibly confined in the high-index or low-index regions for different applications. These enable a wide range of possible applications for the ADB waveguide in several fields, such as improving the efficiency of near-field optical probes [45], avoiding nonlinearity in high-index materials [41], increasing the integration density of optical integrated circuits [4], enhancing fluorescence signals in bioimaging applications [46], and increasing the sensitivity of optical sensing [2].

Acknowledgements This work was supported by the National Key Basic Research Program of China under Grant No. 2012CB922003, and the National Natural Science Foundation of China (NSFC) under Grant No. 61177053, and Anhui Provincial Natural Science Foundation under Grant No. 1508085SMA205.

References

1. R. Kirchain and L. Kimerling, A roadmap for nanophotonics, *Nat. Photonics* 1(6), 303 (2007)
2. F. Dell'Olio and V. M. Passaro, Optical sensing by optimized silicon slot waveguides, *Opt. Express* 15(8), 4977 (2007)
3. K. Nozaki, T. Tanabe, A. Shinya, S. Matsuo, T. Sato, H. Taniyama, and M. Notomi, Sub-femtojoule alloptical switching using a photonic-crystal nanocavity, *Nat. Photonics* 4(7), 477 (2010)
4. T. W. Ebbesen, C. Genet, and S. I. Bozhevolnyi, Surface-plasmon circuitry, *Phys. Today* 61(5), 44 (2008)
5. D. F. Pile and D. K. Gramotnev, Channel plasmon–polariton in a triangular groove on a metal surface, *Opt. Lett.* 29(10), 1069 (2004)
6. V. J. Sorger, N. D. Lanzillotti-Kimura, R. M. Ma, and X. Zhang, Ultra-compact silicon nanophotonic modulator with broadband response, *Nanophotonics* 1(1), 17 (2012)

7. R. F. Oulton, V. J. Sorger, T. Zentgraf, R. M. Ma, C. Gladden, L. Dai, G. Bartal, and X. Zhang, Plasmon lasers at deep subwavelength scale, *Nature* 461(7264), 629 (2009)
8. J. N. Caspers, J. S. Aitchison, and M. Mojahedi, Experimental demonstration of an integrated hybrid plasmonic polarization rotator, *Opt. Lett.* 38(20), 4054 (2013)
9. A. D. Boardman, Electromagnetic Surface Modes, John Wiley & Sons, 1982
10. W. L. Barnes, A. Dereux, and T. W. Ebbesen, Surface plasmon subwavelength optics, *Nature* 424(6950), 824 (2003)
11. J. Wang, A review of recent progress in plasmon-assisted nanophotonic devices, *Front. Optoelectron.* 7(3), 320 (2014)
12. D. K. Gramotnev and S. I. Bozhevolnyi, Plasmonics beyond the diffraction limit, *Nat. Photonics* 4(2), 83 (2010)
13. J. Takahara and T. Kobayashi, Nano-optical waveguides breaking through diffraction limit of light, in: Optics East. International Society for Optics and Photonics, 2004, pp 158–172
14. S. A. Maier, P. G. Kik, H. A. Atwater, S. Meltzer, E. Harel, B. E. Koel, and A. A. Requicha, Local detection of electromagnetic energy transport below the diffraction limit in metal nanoparticle plasmon waveguides, *Nat. Mater.* 2(4), 229 (2003)
15. R. Zia, M. D. Selker, P. B. Catrysse, and M. L. Brongersma, Geometries and materials for subwavelength surface plasmon modes, *J. Opt. Soc. Am. A* 21(12), 2442 (2004)
16. J. B. Khurgin, How to deal with the loss in plasmonics and metamaterials, *Nat. Nanotechnol.* 10(1), 2 (2015)
17. R. F. Oulton, V. J. Sorger, D. Genov, D. Pile, and X. Zhang, A hybrid plasmonic waveguide for subwavelength confinement and long-range propagation, *Nat. Photonics* 2(8), 496 (2008)
18. D. Dai and S. He, A silicon-based hybrid plasmonic waveguide with a metal cap for a nano-scale light confinement, *Opt. Express* 17(19), 16646 (2009)
19. I. Avrutsky, R. Soref, and W. Buchwald, Subwavelength plasmonic modes in a conductor-gapdielectric system with a nanoscale gap, *Opt. Express* 18(1), 348 (2010)
20. Y. Bian, Z. Zheng, Y. Liu, J. Zhu, and T. Zhou, Dielectric-loaded surface plasmon polariton waveguide with a holey ridge for propagation-loss reduction and subwavelength mode confinement, *Opt. Express* 18(23), 23756 (2010)
21. Y. Zhao, and L. Zhu, Coaxial hybrid plasmonic nanowire waveguides, *J. Opt. Soc. Am. B* 27(6), 1260 (2010)
22. Y. Bian, Z. Zheng, X. Zhao, J. Zhu, and T. Zhou, Symmetric hybrid surface plasmon polariton waveguides for 3d photonic integration, *Opt. Express* 17(23), 21320 (2009)
23. L. Chen, T. Zhang, X. Li, and W. Huang, Novel hybrid plasmonic waveguide consisting of two identical dielectric nanowires symmetrically placed on each side of a thin metal film, *Opt. Express* 20(18), 20535 (2012)
24. C. Xiang and J. Wang, Long-range hybrid plasmonic slot waveguide, *IEEE Photon. J.* 5(2), 4800311 (2013)
25. Y. Bian, Z. Zheng, Y. Liu, J. Liu, J. Zhu, and T. Zhou, Hybrid wedge plasmon polariton waveguide with good fabrication-error-tolerance for ultra-deep-subwavelength mode confinement, *Opt. Express* 19(23), 22417 (2011)
26. Y. Bian and Q. Gong, Bow-tie hybrid plasmonic waveguides, *J. Lightwave Technol.* 32(23), 3902 (2014)
27. Z. L. Zhang and J. Wang, Long-range hybrid wedge plasmonic waveguide, *Sci. Rep.* 4, 6870 (2014)
28. Y. Ma, G. Farrell, Y. Semenova, and Q. Wu, Hybrid nanowedge plasmonic waveguide for low loss propagation with ultra-deep-subwavelength mode confinement, *Opt. Lett.* 39(4), 973 (2014)
29. Y. Ma, G. Farrell, Y. Semenova, and Q. Wu, A hybrid wedge-to-wedge plasmonic waveguide with low loss propagation and ultra-deep-nanoscale mode confinement, *J. Lightwave Technol.* 33(18), 3827 (2015)
30. A. Boltasseva and H. A. Atwater, Low-loss plasmonic metamaterials, *Science* 331(6015), 290 (2011)
31. P. Moitra, Y. Yang, Z. Anderson, I. I. Kravchenko, D. P. Briggs, and J. Valentine, Realization of an all-dielectric zero-index optical metamaterial, *Nat. Photonics* 7(10), 791 (2013)
32. D. Lin, P. Fan, E. Hasman, and M. L. Brongersma, Dielectric gradient metasurface optical elements, *Science* 345(6194), 298 (2014)
33. R. Cregan, B. Mangan, J. Knight, T. Birks, P. S. J. Russell, P. Roberts, and D. Allan, Single-mode photonic band gap guidance of light in air, *Science* 285(5433), 1537 (1999)
34. G. Wiederhecker, C. M. B. Cordeiro, F. Couny, F. Benabid, S. Maier, J. Knight, C. Cruz, and H. Fragnito, Field enhancement within an optical fibre with a subwavelength air core, *Nat. Photonics* 1(2), 115 (2007)
35. H. Altug, D. Englund, and J. Vučković, Ultrafast photonic crystal nanocavity laser, *Nat. Phys.* 2(7), 484 (2006)
36. V. R. Almeida, Q. Xu, C. A. Barrios, and M. Lipson, Guiding and confining light in void nanostructure, *Opt. Lett.* 29(11), 1209 (2004)
37. Q. Xu, V. R. Almeida, R. R. Panepucci, and M. Lipson, Experimental demonstration of guiding and confining light in nanometer-size low-refractive-index material, *Opt. Lett.* 29(14), 1626 (2004)
38. V. R. Almeida, Q. Xu, R. R. Panepucci, C. A. Barrios, and M. Lipson, Light guiding in low index materials using high-index-contrast waveguides, in: Materials Research Society Symposium Proceedings, Vol. 797, Cambridge University Press, 2003, pp W6–10

39. P. Müllner and R. Hainberger, Structural optimization of silicon-on-insulator slot waveguides, *IEEE Photonics Technol. Lett.* 18(24), 2557 (2006)
40. A. Turner, I. Karube, and G. S. Wilson, Biosensors: Fun-Damentals and Applications, Oxford University Press, 1987
41. S. P. Singh and N. Singh, Nonlinear effects in optical fibers: Origin, management and applications, *Prog. Electromagnetics Res.* 73, 249 (2007)
42. H. Choi, M. Heuck, and D. Englund, Self-similar nanocavity design with ultrasmall mode volume for single-photon nonlinearities, *Phys. Rev. Lett.* 118(22), 223605 (2017)
43. S. Hu and S. M. Weiss, Design of photonic crystal cavities for extreme light concentration, *ACS Photonics* 3(9), 1647 (2016)
44. J. N. Reddy, An Introduction to the Finite Element Method, New York: McGraw-Hill, 1993, Vol. 2, No. 2.2
45. B. Vohnsen and S. I. Bozhevolnyi, Characterization of near-field optical probes, *Appl. Opt.* 38(9), 1792 (1999)
46. Z. Guo, S. Park, J. Yoon, and I. Shin, Recent progress in the development of near-infrared fluorescent probes for bioimaging applications, *Chem. Soc. Rev.* 43(1), 16 (2014)